Exploring the shear behavior of masonry triplets via digital image correlation, damage quantification and Mohr-Coulomb criterion identification

Louis Collin, Fabrice Gatuingt, Cédric Giry, François Hild

Exploring the shear behavior of masonry triplets via Digital Image Correlation, Damage quantification and Mohr-Coulomb Criterion Identification

Louis Collin[a,b,*], Fabrice Gatuingt[a], Cédric Giry[a,c], François Hild[a]

[a]*Université Paris-Saclay, CentraleSupélec, ENS Paris-Saclay, CNRS, LMPS - Laboratoire de Mécanique Paris-Saclay, 91190 Gif-sur-Yvette, France*
[b]*EDF R&D ERMES, 91120 Palaiseau, France*
[c]*EPF École d'Ingénieurs, 94230 Cachan, France*

Abstract

Shear properties are essential for evaluating the strength of masonry infill walls. Traditionally, shear strength parameters are experimentally determined through triplet shear tests. While extensive research exists on these tests, few studies have combined full-field measurement techniques such as Digital Image Correlation (DIC) with mesoscopic damage analysis and shear strength quantification. Leveraging the detailed displacement fields provided by DIC and force measurements, the study seeks to enhance the characterization of the Mohr-Coulomb criterion in mortar joints. An experimental campaign on eight specimens yields valuable insights through force-displacement curves and DIC post-processing in a monoview configuration. This analysis proposes a novel method to achieve a more precise estimation of triplet shear strength.

Keywords: masonry, triplet shear test, shear strength, virtual gauges, failure criterion

*Corresponding author
Email address: lcollin@ens-paris-saclay.fr (Louis Collin)

Introduction

To accurately predict the structural capacity of masonry walls under in-plane loading, a thorough understanding of their shear stress response is essential. The behavior of masonry is inherently heterogeneous due to its composition, consisting of blocks and joints. Cracks typically form in the joints between blocks [14, 13], but characterizing the mechanical behavior at the joint level remains challenging. Many factors influence the shear strength of a masonry wall [26] such as the material properties—particularly the tensile strength of mortar—and boundary conditions such as, namely, confinement levels [30].

According to the EN 1052-3 standard [33], the triplet shear test setup is widely used in research to evaluate the shear strength of joints [34, 4, 7, 5, 15, 8]. In the test considered herein (Figure 1), the specimen is composed of an assembly of three concrete blocks with two mortar joints. A force F is applied to the central block while the outer blocks are supported, causing a concentration of shear stress in the joint area. Varying levels of confinement σ are applied through horizontal steel rods. This arrangement allows the failure at the mortar-block interface to be studied. In addition, as shown in Figure 1 (right), the experimental setup also allows the cyclic shear response to be investigated [5, 15].

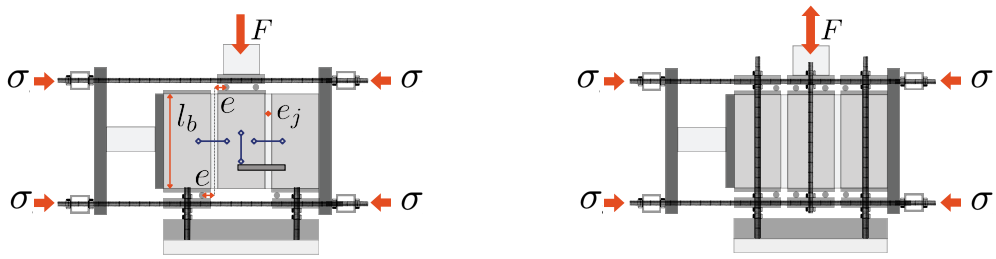

FIGURE 1: Experimental setup for monotonic (left) [33] and cyclic (right) [5] loadings. Adapted from Collin et al. [12].

Despite their widespread use, triplet shear tests present notable limitations. Simultaneous loading of two joints often leads to asymmetric cracking, making the post-peak response difficult to interpret [22, 36]. Alternative setups such as couplet specimens [30] and in-situ shove tests [4] have been proposed to address this challenge. While couplets tend to yield more consistent results and higher parameter estimates, triplet tests remain more representative of real-world conditions, particularly in seismic walls where joints are subjected to forces at both top and bottom interfaces.

A further limitation of traditional triplet tests lies in their instrumentation. These tests typically rely on two Linear Variable Differential Transformers (LVDTs) to assess relative shear displacements and an additional LVDT to monitor the vertical motion of the central block [24, 4, 30, 8]. Although this approach is effective for global measurements, it is limited to discrete points and does not capture the full extent of local damage mechanisms, such as cracking, sliding, or strain localization. To address the previous limitation, Digital Image Correlation (DIC) provides full-field, contactless, and non-intrusive measurements. First applied to masonry by Raffard et al. [25], and later extended to crack propagation studies [31], DIC is now

commonly used in triplet shear tests, particularly to measure kinematic fields and identify crack patterns [8, 6]. Validation studies by Ghorbani et al. [16] and Bompa et al. [7] have shown that virtual gauges derived from DIC data match the accuracy of conventional LVDT measurements.

Building upon the approach of Sciuti et al. [29] on full-scale masonry walls, the novelty of this work lies in advancing the state-of-the-art by using DIC data to study damage development and to provide a macroscopic quantification of damage, rather than just visualizing crack patterns. Applied to triplet shear tests, this methodology enables for the identification of the effective Mohr–Coulomb criterion based on full-field data to quantify the effective shear surface. The triplet shear tests presented herein are parts of a broader experimental framework [11], which integrates DIC-based measurements into shear strength characterization. Achieving reliable results requires careful attention to the experimental setup, including lighting, camera position, and design of the speckle pattern [12]. This study demonstrates how combining full-field DIC measurements with conventional sensor data allows for a more comprehensive and quantitative analysis of the mechanical response of masonry joints under shear loading.

Section 1 begins by describing the experimental campaign and the setup for the triplet shear tests. Section 2 presents the results obtained, starting with the force-displacement curves and followed by post-processing of the digital image correlation data in a monoview setup. In Section 3, a novel method is proposed for a more accurate estimation of triplet shear strength and concludes with a discussion of the results obtained.

1. Experimental campaign

1.1. Virtual testing

The experimental campaign was carefully prepared through a preliminary virtual testing phase [11, 12]. Based on a robust numerical model, a Design of Experiments (DoEs) approach was used to analyze the sensitivity of geometric parameters, namely, block length l_b, joint thickness e_j, support position e (Figure 1), and to select the configuration that is most likely to yield meaningful experimental insights. Regarding the joint thickness, the studied masonry features 2-cm thick horizontal joints and 3-cm thick vertical joints. However, due to the maximum width constraint of the testing machine, a thickness of 2 cm was selected.

The virtual design phase enabled the entire setup to be modeled in Blender [https://www.blender.org/], an open-source animation and rendering software (Figure 2a). This process facilitated the design of the supports and the confinement cell to ensure that they would not obstruct image acquisitions prior to fabrication. The camera and lighting positions were also defined and validated virtually.

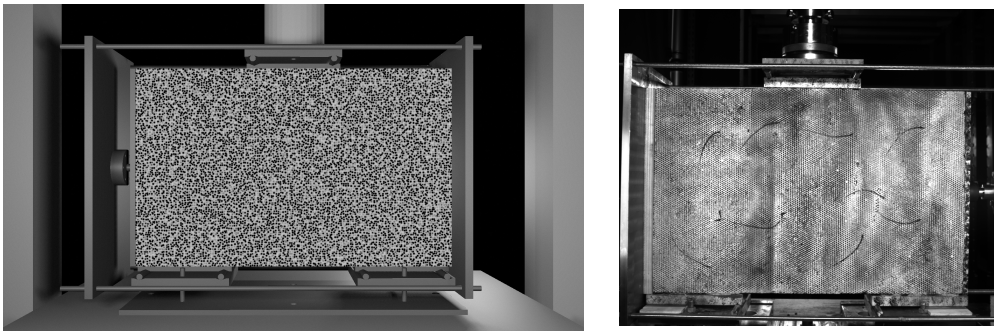

(a) Virtual image (b) Real image

FIGURE 2: Comparison between a virtual image generated in Blender (a) and a real image captured using the experimental setup (b).

The interest of this approach lies in the ability to generate realistic virtual images in Blender, and to *a priori* evaluate measurement uncertainties by simulating the entire acquisition chain. This process notably enables for the optimization of the size of the speckle pattern to minimize measurement uncertainties [12]. Table 1 presents the optimized parameters obtained at the end of this process.

TABLE 1: Parameters optimized through the virtual design phase [12].

Parameters	l_b	e_j	e	d
Values (mm)	400	20	20	2.5

1.2. Brick and mortar characterization

The eight triplets were all constructed identically using solid concrete blocks held together by standard mortar. Each block originally measured 500 mm in length but was cut on both outer faces to achieve a target length of 400 mm. After cutting, the specimens were air-dried and stored in the laboratory for at least 14 days to ensure proper conditioning. Before testing, the blocks were measured and weighed to confirm that they reached a

constant mass. The results of these measurements are shown in Table 2. Some variability in these parameters is evident, although it is not significant. The impact of block length, particularly regarding the force-displacement response, is addressed in a previous study [12].

TABLE 2: Dimensions, weight, and measured density of all concrete blocks, including the indication of standard deviation.

Length (mm)	Width (mm)	Height (mm)	Mass (kg)	Density (kg/m3)
400.6 ± 0.8	190.0 ± 0.4	96.3 ± 0.2	14.9 ± 0.15	2033.4 ± 17.0

Characterization tests were also carried out to determine the mechanical properties of mortar, consisting of lime and cement CP/CEM II B-M-32.5 R with a water/cement ratio of 0.43 by weight. The results of the tests on 40×40×160 mm [32] and 110×220 mm [3, 2, 1] specimens are summarized in Table 3, where E_j and ν_j represent the Young's modulus and Poisson's ratio of mortar, respectively, and $f_{c,j}$, $f_{t,j}$, and $f_{f,j}$ denote its compressive, indirect tensile, and flexural strengths.

TABLE 3: Mechanical parameters of mortar identified through experimental tests, with the corresponding standard deviation.

E_j (GPa)	ν_j	$f_{c,j}$ (MPa)	$f_{t,j}$ (MPa)	$f_{f,j}$ (MPa)
20.7 ± 0.3	0.1 ± 0.01	37.0 ± 3.9	3.37 ± 0.6	4.6 ± 2.1

1.3. Manufacturing of masonry triplets

Eight triplets were tested, with each triplet consisting of a single row of solid blocks. Each triplet included a stack of three solid blocks and two target joint thicknesses of 2 cm. The resulting samples had uniform dimensions

of approximately 400.6 × 610 × 96 mm. These assemblies were kept in a controlled atmospheric environment under a 10 kg load for 28 days. After the curing period, they were tilted to a 90° position for shear testing (see Figure 3a).

1.4. Experimental setup

Shear tests were conducted using a Zwick/Roell Z100 universal testing machine with a 100kN capacity, coupled with a 50 kN load cell capable in a horizontal position to measure the real-time constraining force perpendicular to the bed joints of the tested samples (Figure 3a). Before testing, the specimens were surfaced and speckled to optimize the image correlation rendering. The bottom support plates were previously bonded with Sykadur glue to ensure that the specimen was supported only on the support cylinders. At the top, the support plate was simply held in place by force.

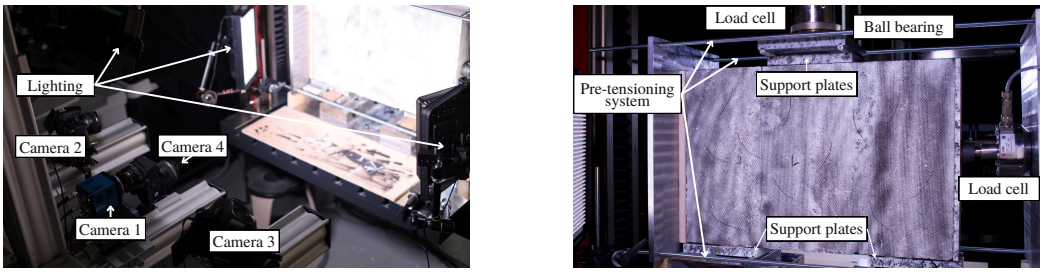

(a) Experimental setup

(b) DIC setup

FIGURE 3: Experimental (a) and DIC (b) setup for the triplet shear tests.

Five 8-bit digital cameras were placed at different locations near the points defined in Blender [12], without tilting, to monitor different zones of the sample surface (Figure 3b). The positioning of the light sources was also taken into account. The first three cameras captured the entire specimen

area, while the fourth camera zoomed in on the left joint zone. The fifth camera observed the opposite side and was positioned symmetrically with Camera 1 relative to the tested specimen. Reflections were minimized by painting the steel supports black. In this paper, only cameras 1 and 5 are used; therefore, the focus is solely on the monoview image correlation setup. Table 4 summarizes the hardware parameters of the current monoview setup.

(a) Speckle pattern sprayed on the specimen

(b) PCO.edge camera

FIGURE 4: Speckle pattern (a) and PCO.edge camera (b) for the triplet shear tests.

TABLE 4: DIC hardware parameters for triplet shear tests

	Camera 1	**Camera 5**
Camera type	PCO.edge 5.5 USB 3.0 (Figure 4b)	
Definition	2560 × 2160 px	2560 × 2160 px
Color filter	none	none
Gray Levels rendering	8 bits	8 bits
Lens	Nikon EF 24 mm	Nikon EF 24 mm
Aperture	f/2.8	f/2.8
Field of view	610 mm × 401 mm	610 mm × 401 mm
Image scale	0.29 mm/px	0.27 mm/px
Stand-off distance	∼ 1.25m	∼ 1.2m
Image acquisition rate	1/7 fps	1/7 fps
Patterning technique	B/W paints	B/W paints
Mean pattern feature radius	3.9 px	4.0 px

When using two or more cameras for measurement purposes, synchronization between them is crucial. Any time lag between cameras may lead to errors in DIC measurements. Due to transfer limitations, an acquisition rate of one image every 7 s was selected for both cameras. However, the force measurements were performed at a higher frequency. Each force data point is linked to the number of images acquired last to ensure synchronization. This coupling allows one to determine the force applied when the n-th image series was captured.

To quantify measurement uncertainties, the two cameras captured another sequence of 50 images of the reference configuration beforehand. Figure 5 illustrates the test procedure for the triplet shear test using DIC.

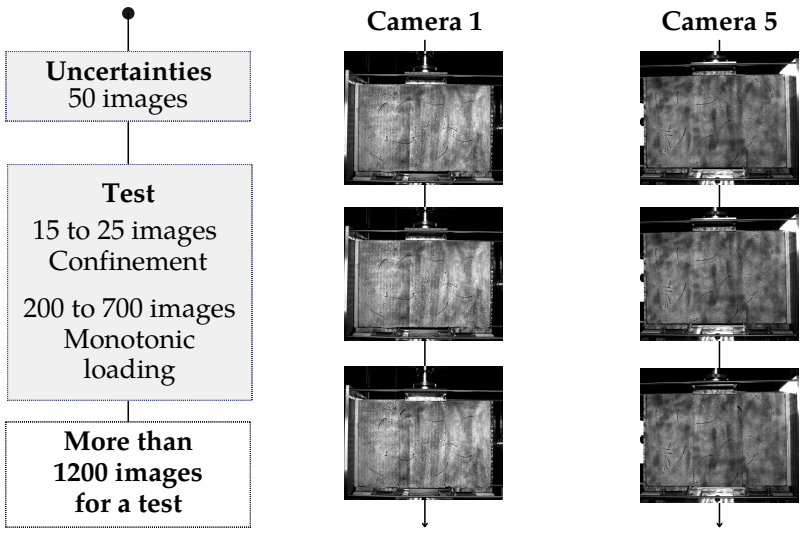

FIGURE 5: Test Procedure for triplet shear tests with monoview DIC.

The speckle pattern applied to the specimen (Figure 4a) was designed to facilitate comprehensive monitoring of the entire displacement field of the

triplet. Selecting the appropriate dot diameter required a careful balance; specifically, the speckle size needed to be sufficiently fine to achieve the spatial resolution necessary to study crack propagation while also being large enough to ensure accurate measurements in the presence of acquisition noise. The virtual design phase indicated that a grid with a dot diameter of 2.5 mm represented the optimal compromise for this particular case [12]. An initial regular pattern was created using a 2 mm grid, followed by applying black paint, resulting in more than 1,500 dots (Figure 4a). Finally, random stripes were added to introduce variability into the pattern.

1.5. Loading

The test was displacement-controlled with a prescribed speed of 1 μm/s. The experiments were carried out with four different pre-compressive stresses σ. The chosen pre-compression levels were within the range of the EN 1052-3 standard [33]. The pre-compressive stress was applied using two steel plates held together by four steel rods. The plates moved closer together by tightening the nuts, increasing the constraining force, measured by a spherical load cell. During the application of the pre-stress, images were captured to measure the prescribed displacements along the entire boundary. A total of four different specimen configurations were defined. Table 5 summarizes the characteristics of the tested specimens and the loading levels.

TABLE 5: Tested Specimens - Shear Test.

Test	**Length** (mm)	**Height** (mm)	**Depth** (mm)	**Pre-compression** σ (MPa)
TRIPLET_1	400.8	609.5	96.1	0.2
TRIPLET_2	401.5	610.2	96.3	0.07
TRIPLET_3	400.2	608.7	96.6	0.07
TRIPLET_4	401.3	610.4	96.1	0.04
TRIPLET_5	400.7	610.2	96.2	0.04
TRIPLET_6	399.2	609.7	96.5	0.09
TRIPLET_7	400.6	610.3	96.3	0.09
TRIPLET_8	400.2	610.7	96.3	0.09

2. Monotonic triplet shear tests

Triplet shear tests were equipped with two load cells, and monoview DIC was performed on both sides of the specimen. Following the presentation of the force-displacement curves, this paper introduces the monoview DIC formulation and the full-field results obtained from the tests.

2.1. Force results

The results of the shear tests are shown in Figure 6. The displacement corresponds to the target position of the crosshead. The blue curve illustrates the force applied by the actuator, while the orange curve depicts the variation in constraining force throughout the test. These curves begin after an initial pre-compression phase is applied using steel bars.

The TRIPLET_1 test remained within the elastic range until it reached the maximum force limit of the testing machine (100 kN), as seen in Figure 6a. However, small discontinuities began to appear in the displacement field, which were observed using Digital Image Correlation (DIC), as shown in

Figure 7a. It is worth noting that during the elastic phase, the constraining force remained constant. In contrast, for all other tests, the constraining force experienced a sudden change when a crack initiated and continued to increase thereafter. This behavior is explained by the fact that the opening of the crack caused dilatancy, meaning that the blocks began to separate and exert additional pressure on the confinement casing. Once cracking occurred, the sample was subjected to larger displacements to evaluate its residual shear strength [4]. This residual strength is attributed to friction generated by the compressive force. During this phase, relative slip occurred between the two parts of the assembly along the crack plane.

The TRIPLET_2 and TRIPLET_3 tests for a pre-compression of 0.07 MPa were quite similar to those observed in the literature [5], with cracking occurring first in one joint. In the case of TRIPLET_2, the crack propagated throughout the height of the first joint at a displacement of 2 mm, and then in the second joint at approximately 3 mm, leading to a brittle failure followed by a convergence to a residual regime (Figures 6b and 7b). It is noteworthy that the loss of force after the first crack was relatively small, unlike the TRIPLET_3 test, where the force drop was much more significant at 1.8 mm, followed by a recovery of force and finally a compressive failure in the footing of the right block at 2.5 mm (Figures 6c and 7c). This failure mode hinders any reliable residual behavior analysis, as frictional effects no longer govern the observed behavior.

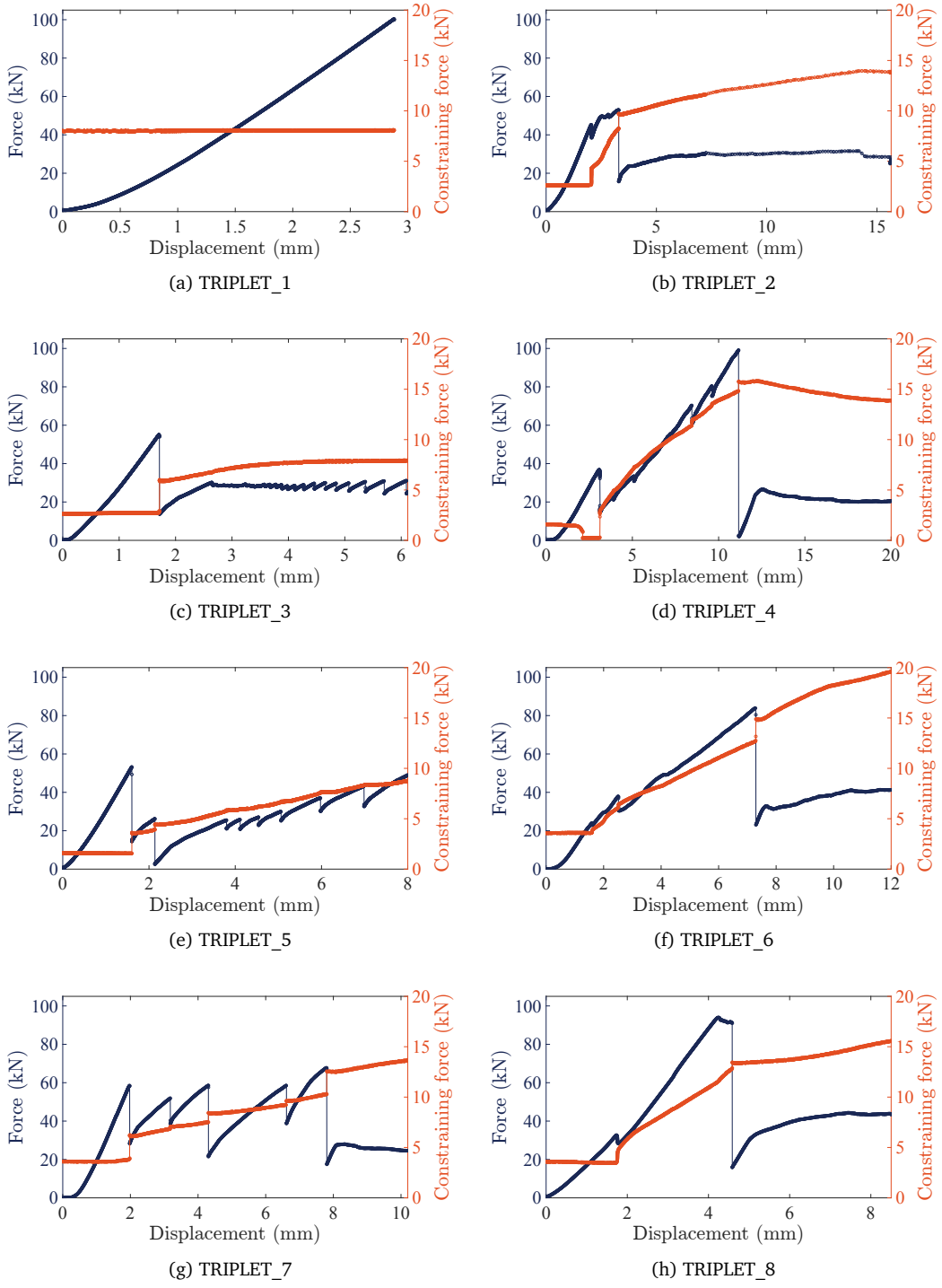

(a) TRIPLET_1 (b) TRIPLET_2

(c) TRIPLET_3 (d) TRIPLET_4

(e) TRIPLET_5 (f) TRIPLET_6

(g) TRIPLET_7 (h) TRIPLET_8

FIGURE 6: Force-displacement curves for each triplet shear test (in blue), with the change of the constraining force (in orange).

The TRIPLET_4 and TRIPLET_5 tests, conducted with a lower pre-compression level of 0.04 MPa, present additional challenges in the analysis. The applied force was experimentally relatively low, making it difficult to maintain it constant. In the TRIPLET_4 test, a gradual drop in the measured constraining force was observed, initially attributed to insufficient initial tightening (Figure 6d). However, a post-test analysis using DIC revealed a weakness in the upper part of the right joint. This local weakness may have led to a reduction in the constraining force. The first joint cracked at a consistent load of approximately 40 kN, which is then followed by a significant increase in constraining force as the cracks opened. The second joint cracked at a much higher force, nearing 100 kN. A different crack pattern was observed compared to previous tests, with through-cracking in mortar, indicating a cohesive shear failure (Figure 7d). In the case of the TRIPLET_5 test, a single crack formed in the joint at 1.7 mm, followed by compressive failure in the footing of the block bonded to the steel support with Sykadur glue (Figures 6e and 7e).

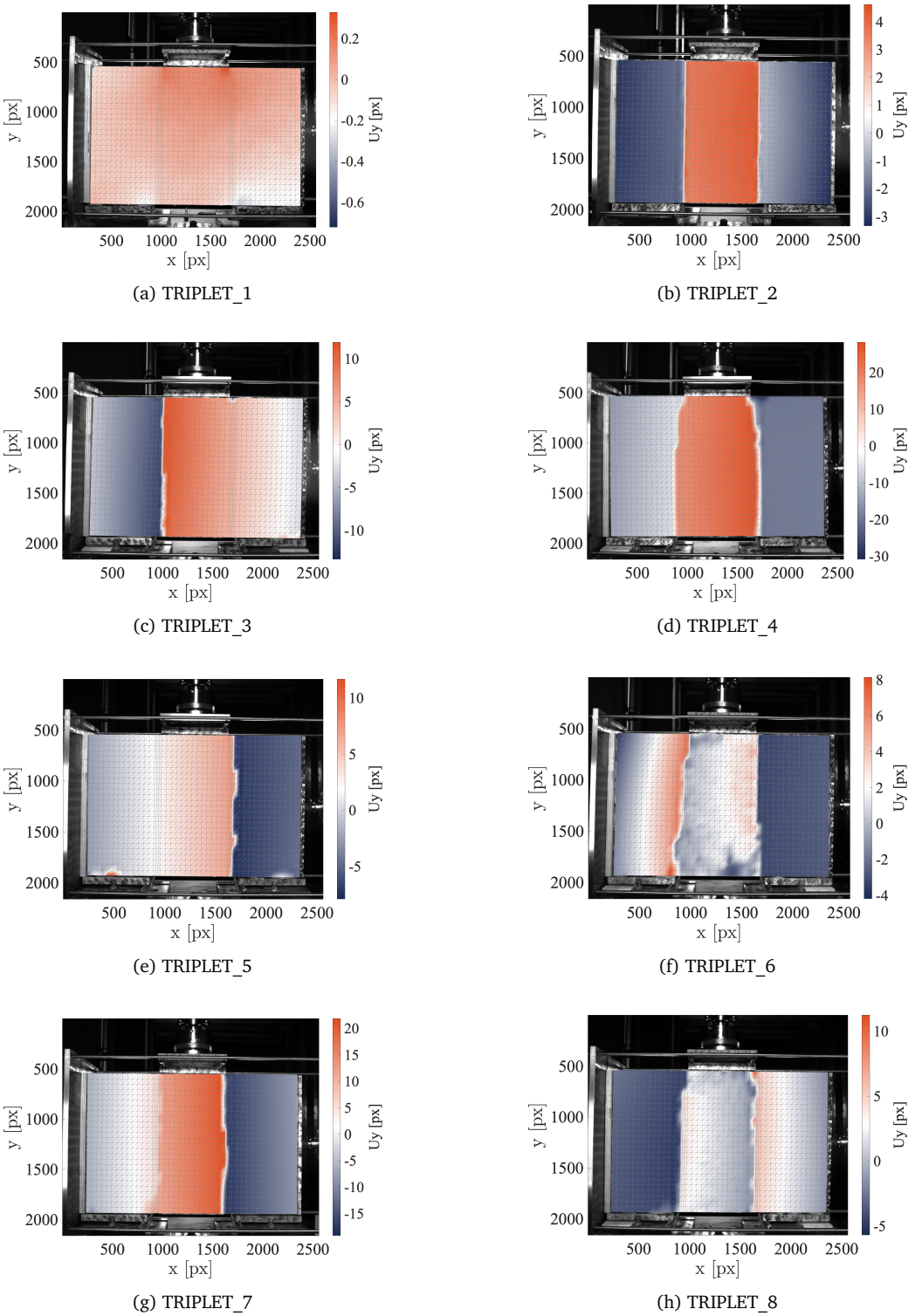

(a) TRIPLET_1

(b) TRIPLET_2

(c) TRIPLET_3

(d) TRIPLET_4

(e) TRIPLET_5

(f) TRIPLET_6

(g) TRIPLET_7

(h) TRIPLET_8

FIGURE 7: Types of failure for each triplet shear test deduced from vertical displacement fields (1px $\sim$ 0.3mm).

For the TRIPLET_6, TRIPLET_7, and TRIPLET_8 tests, conducted with a pre-compression of 0.09 MPa, the results were consistent, as the maximum failure forces achieved were the highest. In the TRIPLET_6 and TRIPLET_8 tests, initial cracking began below 40 kN; however, the higher constraining force prevented any significant force drop until complete cracking occurred in both joints, at forces exceeding 80 kN (Figures 6f and 6h). In both cases, cohesive failures crossing the joint were observed, with the failure even extending into the left block in the TRIPLET_6 test (Figures 7f and 7h). In the TRIPLET_7 test, a compressive failure occured in the block footing at the supports after an initial crack formed in one joint. The second joint subsequently cracked at around 70 kN, though with altered boundary conditions (Figures 6g and 7g).

2.2. Preparation for DIC Calculation

In this section, the analysis focuses on the TRIPLET_2 test, applying the same methodology to the other tests as well. The results differ among tests, as they depend on the specific failure mode observed in each case. However, the data from all eight tests will be collectively analyzed in Section 3.2 to determine the Mohr–Coulomb failure criterion, which constitutes the main novelty of this study.

Digital Image Correlation (DIC) is a full-field method to measure displacement fields by registering images at different time instants [17, 9]. This technique analyzes two images of the same object under different loading conditions. The main objective is to determine the displacement field $\mathbf{u}(\mathbf{x})$ that leads to the best match between the reference image f and the deformed image g. It is based on the principle of gray level conservation

during the deformation process [17]. As early as 1981, Horn and Schunck provided a robust formulation of this concept [20]

$$\forall \mathbf{x} \in R, f(\mathbf{x}) = g(\mathbf{x} + \mathbf{u}(\mathbf{x})) \tag{1}$$

where $R \subset \mathbb{R}^2$ denotes the Region of Interest (ROI). The Correli 3.2 framework, developed at LMPS [21], was used in this study to measure displacement fields $\mathbf{u}(\mathbf{x}, t)$. This library offers a platform for implementing DIC codes in Matlab. All the equations of the global formulation used herein are detailed in Appendix A. Table 6 gathers the monoview DIC parameters for both cameras.

TABLE 6: Monoview DIC analysis parameters for cameras 1 and 5 (TRIPLET_2).

Parameter	Camera 1	Camera 5
DIC software	Correli 3.2 [21]	
Image filtering	None	
Element sizes	$\sim$ 47 px	$\sim$ 46 px
Shape functions	Linear (T3 elements)	
Matching criterion	Regularized sum of squared differences (A.5)	
Regularization length	50 px	
Interpolant	Spline	
Displacement noise-floor	0.04 px	0.05 px

2.2.1. Projection of the FE Mesh

The main advantage of the global DIC formulation lies in its ability to align experimentally measured displacement fields with those predicted by Finite Element (FE) simulations. While this test-calculation interaction will not be addressed herein, it is planned for future work, with the aim of identifying nonlinear parameters from the data measured during the tests.

In this context, one face of the 3D FE mesh (Figure 8a) is projected onto the 2D surface of the specimen surface (Figure 8b) by aligning the mesh corners with the four corners of the specimen. The elements in mortar have an average size of 6 mm, which allows for approximately three elements across the thickness of each mortar joint. For the blocks, the element size is increased to 15 mm. The scale factor for each camera is then determined as the ratio between the size of the mesh elements in meters and their size in pixels. Last, the quadrilateral elements are converted into triangular elements for the DIC calculations [21].

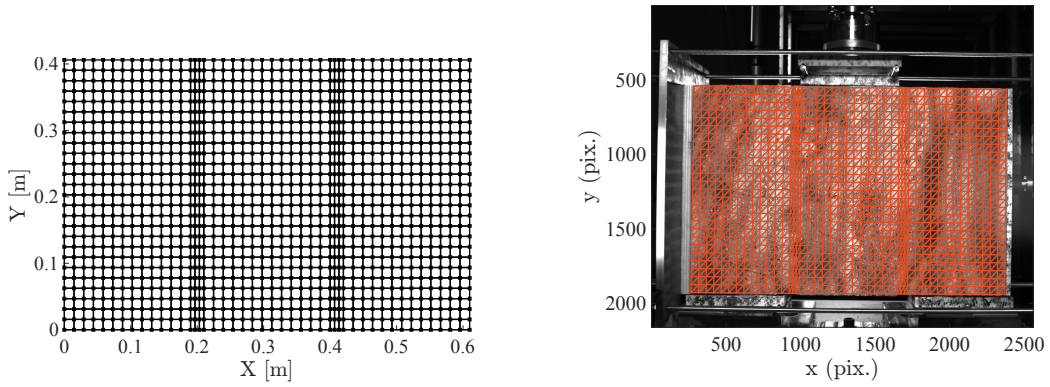

(a) FE Mesh

(b) Front camera

FIGURE 8: Projection of the FE Mesh (a) onto the specimen surface for camera 1 (b).

2.2.2. Uncertainty quantification

To assess measurement uncertainties using DIC, 50 images were acquired without any applied loading (Figure 5). For each node in the defined mesh, the displacements obtained from the DIC measurements is evaluated, reflecting the measurement uncertainty. The standard uncertainty at each node is calculated by determining the standard deviation of the displacements measured in this set of images. Figure 9a illustrates how the element length

affects DIC uncertainties. As the element size decreases, the measurement uncertainty increases due to the smaller evaluation area, highlighting the well-known trade-off between measurement uncertainty and spatial resolution [19]. Conversely, when mechanical regularization is applied (e.g., with a regularization length of ℓ_{reg} = 50 px), the standard displacement uncertainties are reduced for elements smaller than the regularization length [29]. In the case of the FE mesh, the length of the smallest elements at the joint is approximately 20 px. Figure 9a demonstrates the benefits of mechanical regularization. The displacement uncertainty field $\boldsymbol{\gamma}_u$ calculated for the FE mesh with a mechanical regularization length of 50 px is displayed in Figure 9b. This approach ensures that mechanical regularization prevents a significant increase in standard uncertainty for nodes near the joints. In contrast, the uncertainty field remains relatively smooth, with an increase observed near the edges of the specimen—a common characteristic in DIC. However, these higher values remain relatively low compared to the measured displacement fields during testing, reaching 0.2 px when cracking occurs (see Figure 12).

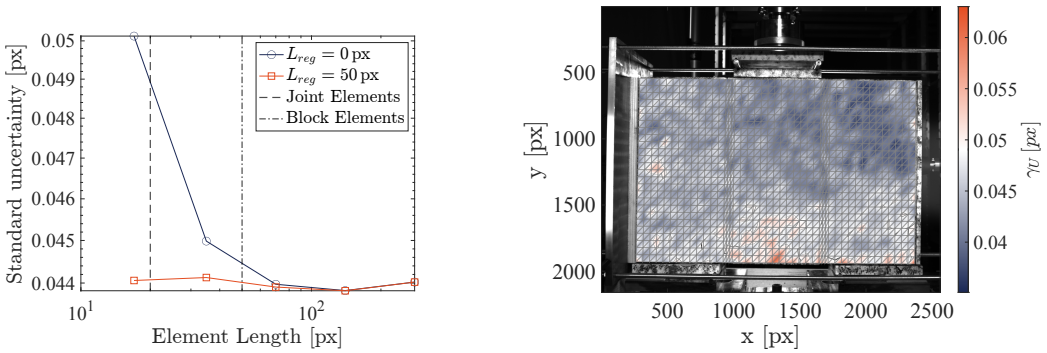

FIGURE 9: Standard uncertainties related to horizontal displacement influenced by the regularization length (a) and DIC uncertainties for the finite element mesh with a regularization length of 50 px (b) for camera 1.

2.2.3. Force-based selection of photos

The challenge in DIC is to accurately capture specific events, such as cracking within mortar. To achieve this, it is important to take as many images as possible during the test. However, processing all these images can be computationally expensive. Therefore, a method is proposed to select the images used in the DIC calculations by analyzing the force-displacement curve. The developed code detects local peaks in the force-displacement curve and refines image selection around these peaks to effectively track drops in force (see Figure 10a). In the absence of detected peaks, an image is chosen every 30 increments. This approach facilitates efficient data management and ensures that critical events, such as cracks or other significant changes in material response, are captured without overwhelming the computational process. For the TRIPLET_2 test, this method reduced the total number of processed images from 838 to 104 (refer to Figure 10b).

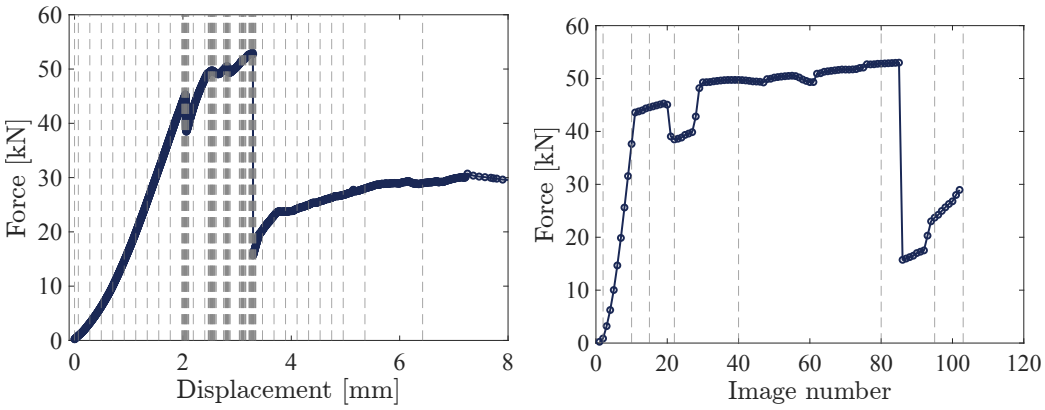

(a) (b)

FIGURE 10: (a) Force-based selection of images for DIC analysis. The dashed lines indicate the instants at which selected images were taken. (b) Change of the shear force as a function of the image number. The dashed lines represent the images that will be analyzed in the subsequent section.

2.2.4. Damage development

Mechanical regularization helps distribute the strains across the mesh. To accurately capture higher displacement gradients, local damage is introduced that relaxes the regularization in specific areas [29]. Initially, a Digital Image Correlation (DIC) calculation was performed on all the images. An element is classified as damaged if the gray-level residuals from a given image (defined in Equation (A.4)) exceed six times the associated uncertainty. Its stiffness matrix is then degraded by multiplying by $(1 - D_0)$. Figure 11 shows the front camera's first image with damaged elements. Notably, the damaged elements are predominantly located in regions corresponding to mortar or its interface with the concrete blocks, which aligns with expected damage patterns. Cracking first occurs in the right joint between image indices 20 and 40, while cracking in the left joint appears around image index 90.

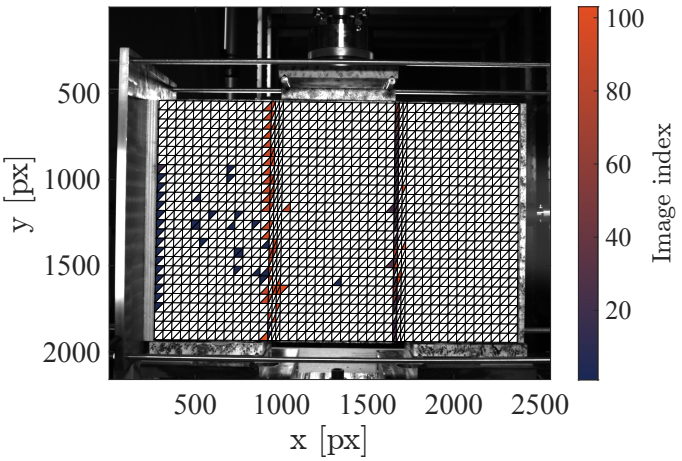

FIGURE 11: Map of first image for which elements were damaged. If damage never occurred, the element remains white.

The parameter D_0=0.9 was selected to reduce the regularization weight in damaged elements [29]. This choice was based on two opposing considerations. On the one hand, if D_0 is not high enough, it becomes difficult to relocalize the strain field, which may cause damaged areas to spread across several neighbouring elements. On the other hand, if D_0 is set too high, achieving convergence of the DIC code for the final images becomes more challenging.

2.3. Monoview DIC results

After the previous steps, which prepared the DIC calculations, the images taken during the confinement phase and the test itself are now discussed.

2.3.1. Full-field measurements

DIC's primary advantage lies in its capability to measure displacement fields for each image in relation to a reference image captured before applying confinement to the sample. The displacement fields are reported

after the removal of any rigid body motion. In step 2, only the constraining force was applied to the specimen, resulting in a gradient field along the X direction (Figure 12). This confinement also induced a slight rotation, which is especially noticeable in the U_Y displacement field. Monotonic loading then began, and at increment 10 (F = 25.6 kN), the U_Y displacement field looks like a bending pattern, with the displacement field remaining continuous at this stage. At increment 15 (F = 43.9 kN), the first discontinuities appeared at the two joints, although at a relatively low amplitude. At increment 22 (F = 45.1 kN), the horizontal displacement maps reveal significant gradients, indicating the presence of a crack in the right mortar region, which was initiated at the bottom of the specimen. This crack continued to propagate vertically along the height of the sample, progressing until increment 40 (F = 49.7 kN) (Figure 13). At this stage and at increment 80 (F = 52.9 kN), a rotation of the two left blocks is observed in the displacement fields. At increment 95 (F = 20.3 kN), the left joint also fractured. This event marks the transition to the residual regime, where the central block begins to move downward while sliding against the two adjacent blocks that rest on the supports.

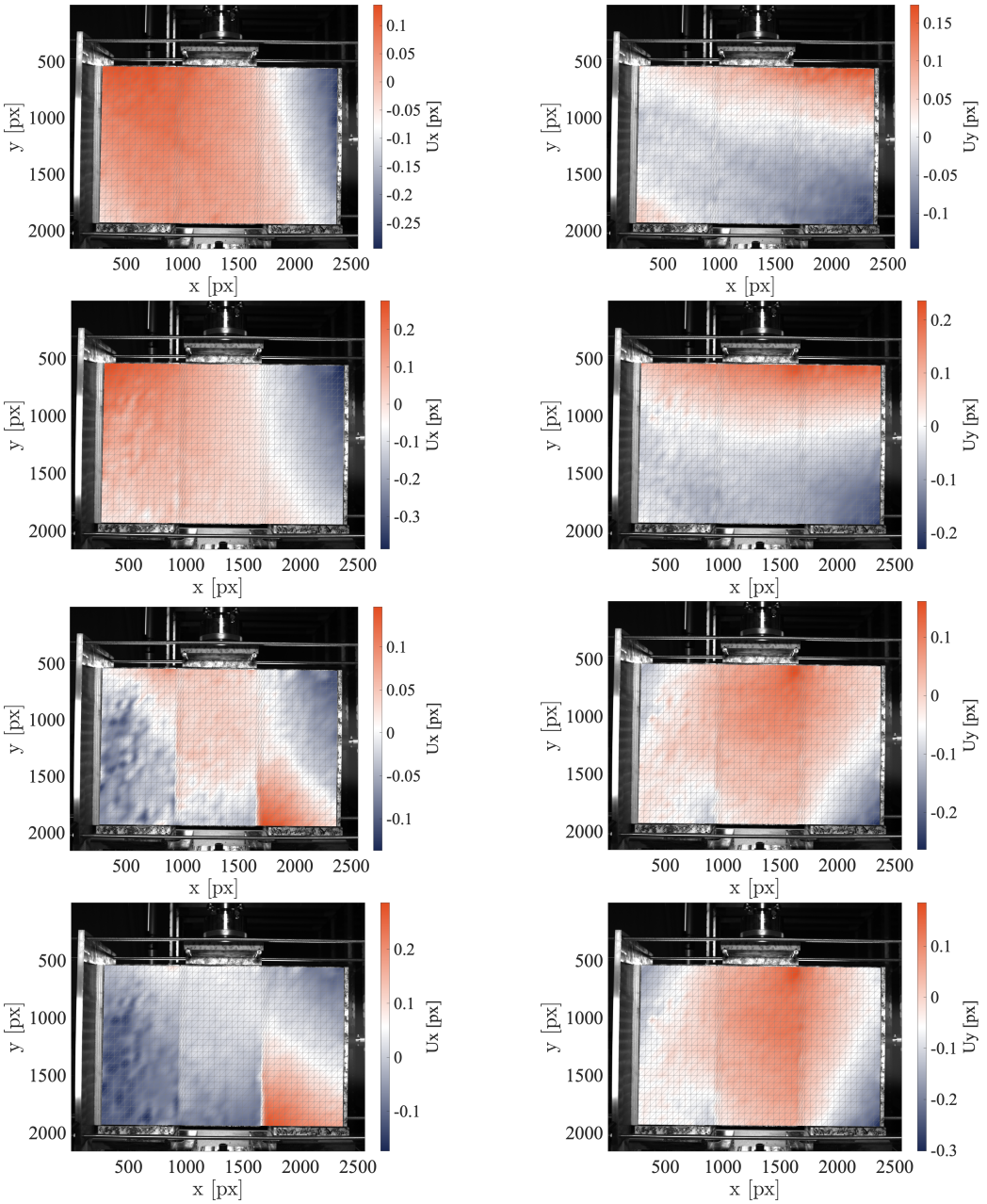

FIGURE 12: Displacement fields for X- (left) and Y- (right) direction, at increments 2, 10, 15, 22 (from top to bottom).

Plotting the Brightness and Contrast fields associated with the BCCs is

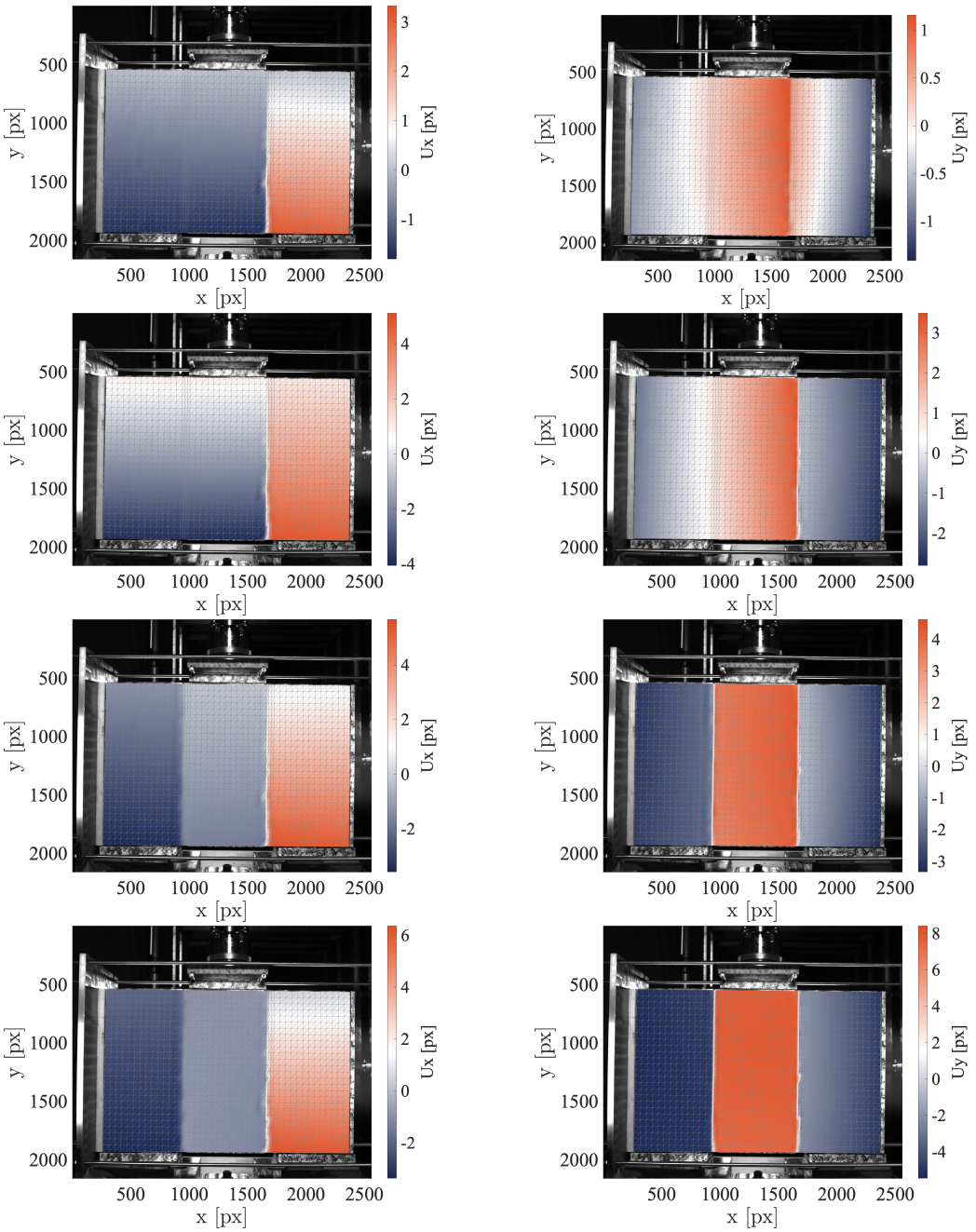

FIGURE 13: Displacement fields for X- (left) and Y- (right) direction, at increments 40, 80, 95, 103 (from top to bottom).

also beneficial to check the values and ensure no spurious local artifacts were present (Figure 14). For this analysis, the BCC regularization length was set to a high value of 320 px. With lower regularization, it was observed that the B and C fields mitigated cracking.

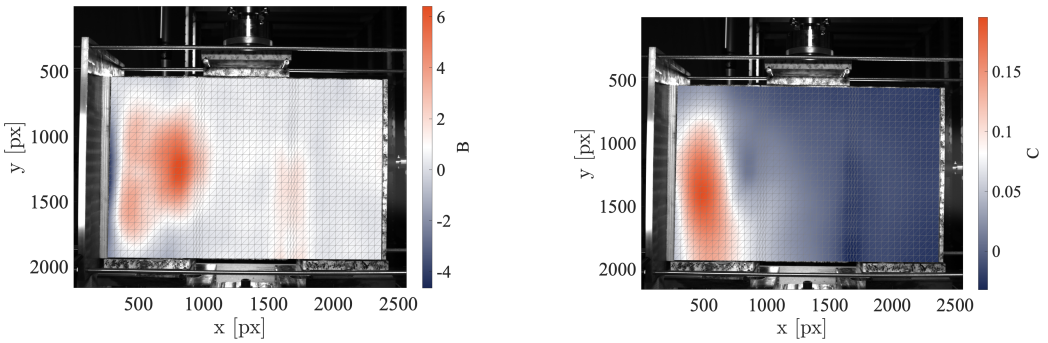

(a) Brightness (b) Contrast

FIGURE 14: Brightness (a) and contrast (b) correction fields at increment 40.

2.3.2. Virtual gauges

The DIC measurements are now compared with those commonly obtained using analogue sensors in triplet shear tests. Previous validations by Ghorbani et al. [16] and Bompa et al. [7] have shown that DIC achieved accuracy comparable to that of LVDTs in such tests. Figure 15a illustrates the standard placement of LVDTs: one vertical LVDT to measure the displacement of the central block relative to the end blocks and two horizontal LVDTs to capture the expansion of the joints. As discussed in the previous subsection, DIC provides full-field displacement measurements, eliminating the need for the vertical LVDT. The goal now is to use the DIC data to also measure the expansion of the joints.

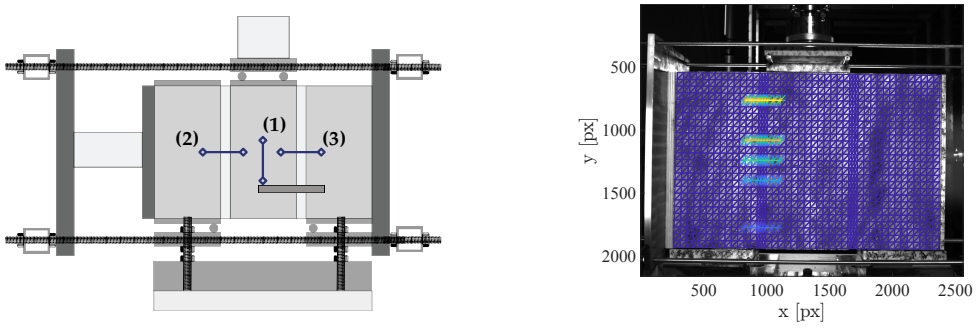

(a) (b)

FIGURE 15: Instrumentation of the Triplet Shear Test with Conventional Gauges (a) or with virtual gauges (b) using DIC data.

Starting from the FE mesh, it is possible to define virtual gauges (as illustrated in Figure 15b). In practice, a virtual gauge is defined for each line of nodes in the mesh for both joints. The expansion of the joints measured by the virtual gauges is calculated as the difference in X-direction displacements between the two extreme points, similar to the operation of a classical extensometer. The plots of the surfaces shown in Figure 16 are derived for the both joints as functions of time and the Y-coordinate of the virtual gauge in the reference frame of the Finite Element Mesh (Figure 8a).

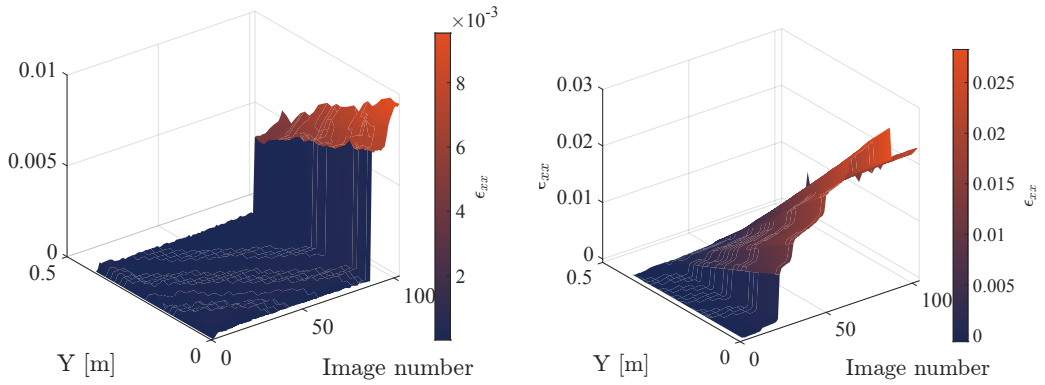

(a) Left joint (b) Right joint

FIGURE 16: Evolution of horizontal strain over time and along height Y for the left joint (a) and right joint (b).

DIC offers the advantage of enabling multiple measurements in these areas and facilitates the visualization of strain fields ϵ_{xx}. The heterogeneity of this field along the joint height in the Y-axis direction is visible, especially for the right joint. The crack opening within the joint is indicated by a strain jump, which may be abrupt (for the left joint) or gradual (for the right joint), with the crack propagating from the bottom to the top of the mesh. These findings highlight the benefits of DIC measurements, which provide enhanced visualization of underlying phenomena that may be missed by local measurements alone.

2.4. Crack opening and macroscopic damage quantification

Upon convergence, elementary strains are obtained via exact differentiation of shape functions. The maximum principal strain, ϵ_1, is commonly used to characterize crack networks [18], regardless of orientation or cracking mode. In cracked regions, elastic strains are assumed to be negligible compared to the singular contributions from cracks. The mean strain tensor

for each element e within its domain Ω_e and its boundary Γ_e is defined as [28]

$$\bar{\boldsymbol{\epsilon}} \approx \frac{1}{|\Omega_e|} \int_{\Gamma_e} [\![\mathbf{u}(\mathbf{x})]\!] \otimes \mathbf{n}(\mathbf{x}) \, \mathrm{d}s \tag{2}$$

The Mean Crack Opening Displacement (MCOD) is computed from the mean strain tensor [28, 29]

$$[\![\bar{\mathbf{u}}]\!] \otimes \bar{\mathbf{n}} = \frac{1}{|\Gamma_e|} \int_{\Gamma_e} [\![\mathbf{u}]\!] \otimes \mathbf{n} \, \mathrm{d}s \tag{3}$$

where $\bar{\mathbf{n}}$ is the mean crack normal. The maximum principal strain ϵ_1 is linked to the MCOD by

$$|\Omega_e| \bar{\boldsymbol{\epsilon}}_1 = |\Gamma_e| [\![\bar{\mathbf{u}}]\!] \tag{4}$$

For small element sizes, where each element contains a single crack, the ratio $|\Omega_e|/|\Gamma_e|$ scales with the element size ℓ. Throughout the remainder of the study, the MCOD is so approximated as

$$[\![\bar{\mathbf{u}}]\!] = \ell \bar{\boldsymbol{\epsilon}}_1 \tag{5}$$

Figure 17a illustrates the change of the cumulative MCOD for all mesh elements, as well as for elements specifically in the left and right joints. A gradual increase in MCOD is observed initially in the right joint, followed by a sudden increase in crack opening in the left joint. At the end of the test, the total crack openings in both joints are similar. Figure 17b shows

the change of the cumulative MCOD per band of elements in the right joint. The results are consistent with those of Figure 16, displaying a progressive crack opening, with higher MCOD levels initially in the lower part of the joint (lower Y) that subsequently increase along the entire height.

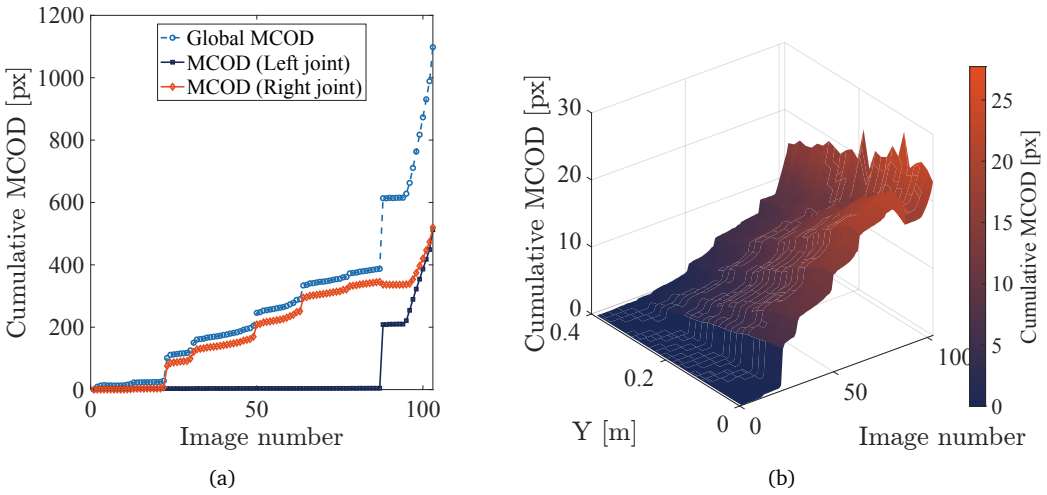

(a) (b)

FIGURE 17: Changes of the cumulative MCOD (a) and Cumulative MCOD over time and along the height Y for the right joint (b).

The previous discussions provided valuable insights into crack initiation and propagation in the specimen during triplet shear tests. However, the selected ranges did not allow for a complete quantification of crack openings. The current objective is to achieve a macroscopic damage quantification for each test. To accomplish this, Sciuti et al. [29] introduced two key metrics: the MCOD in damaged elements and the Surface Crack Density (SCD), which is defined as the ratio of the damaged area divided by the total area of the specimen. In the case of triplet shear tests, the focus is on studying these quantities for all elements in the mesh or those close to the joints. Both quantities are displayed in Figure 18.

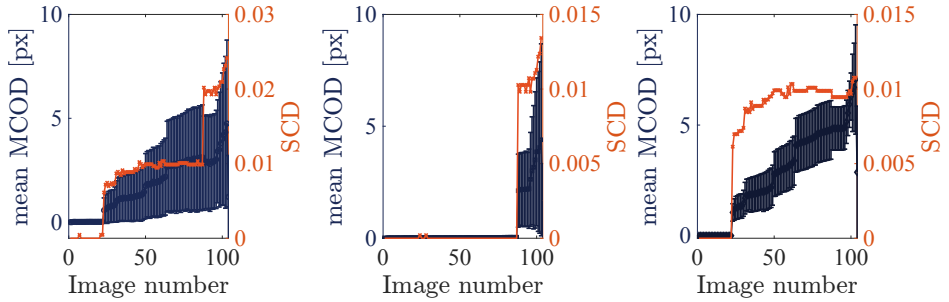

FIGURE 18: Mean MCOD (blue) with standard deviation (error bars) and SCD (orange) as functions of image number for damaged elements of all the specimen (left), near the left joint (middle), and near the right joint (right).

As expected from the previous results, a sudden increase in the mean MCOD at index 22 (F = 45.1 kN) corresponds to the first crack initiation. The mean MCOD then increases slightly up to index 87 (F = 53.0 kN) with the second crack initiation. One can zoom in on the images of interest around the crack initiation (Figure 19). It is noteworthy that two distinct regimes are observed between the two joints. For the left joint, the increase in the mean MCOD is sudden, rising from 0 to 2.2 px in just one image, which suggests an adhesive phenomenon along the interface between mortar and the block. In contrast, the evolution of the mean MCOD for the right joint occurs in steps, with a more gradual increase. Twenty images after cracking, the mean MCOD is only 2 px, which is still lower than the value found for the left joint. Similar results are observed regarding the evolution of SCD , with more progressive damage to the right joint. This observation suggests a mixed adhesive-cohesive phenomenon and is confirmed after the experiment by a much rougher fracture surface for the right joint compared to the left one. The displacement fields shown in Figure 13 also reveal less straight cracking in the right joint, in contrast to the left joint.

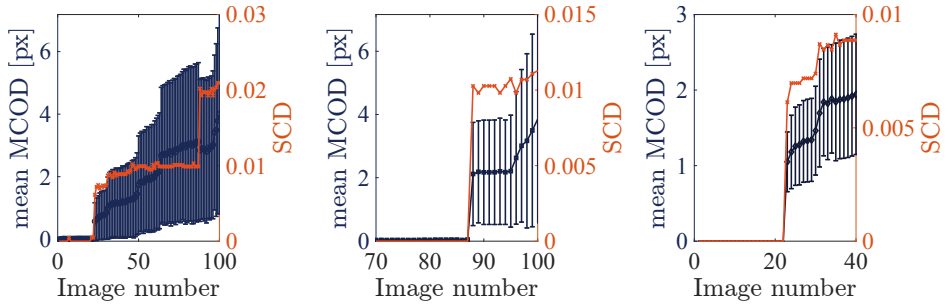

FIGURE 19: Mean MCOD (blue) with standard deviation (error bars) and SCD (orange) as functions of specific image number for damaged elements of all the specimen (left), near the left joint (middle), and near the right joint (right).

To further analyze the histories of mean MCOD and SCD, these quantities are plotted as functions of the constraining force applied to the specimen (Figure 20). Regarding the evolution of the SCD, it is noteworthy that it occurs in discrete steps. The constraining force increases from 2.5 to 4 kN during the first cracking event, accompanied by an SCD increase from 0 to 0.01. A plateau follows this trend. The constraining force continued to rise up to 8 kN with no further increase in SCD. At 9 kN, the second cracking event occurred, resulting in another rise in SCD, which reached 0.025. In contrast, the mean MCOD following each cracking event appears to be more linear with respect to constraining force up to 8 kN. This response is attributed to damage to the elements occurring rapidly during cracking. However, the opening of the cracks at the joints continued to increase, leading to a gradual increase in constraining force.

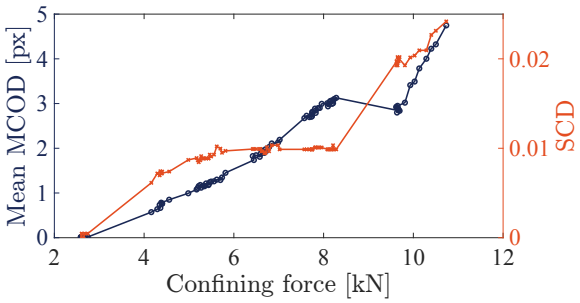

FIGURE 20: Mean MCOD (blue) and SCD (orange) as functions of the constraining force.

These analyses highlight the value of combining force measurements with full-field data obtained through DIC to gain a more comprehensive understanding of the behavior of mortar joints in masonry. Building on the previous analyses, the objective is now to propose a new method to better identify the parameters involved in a Mohr-Coulomb criterion.

3. Identification of Mohr-Coulomb parameters

A standard approach for analyzing masonry triplet tests is to use the Mohr-Coulomb failure criterion. This method is widely used in numerical studies [4], as once the crack propagates from top to bottom, friction due to sliding is observed on either side of the crack, which is influenced by the level of confinement [5, 7, 15].

3.1. Normative approach

For each test, the EN 1052-3 standard defines the shear stress τ and the confining stress σ using the following expressions [33]

$$\tau = \frac{F_{i,peak}}{2A_i} \; ; \; \sigma = \frac{F_{i,p}}{A_i} \tag{6}$$

where $F_{i,peak}$ represents the maximum force reached, $F_{i,p}$ is the constraining force, and A_i is the lateral surface area of $401 \times 96\,\text{mm}^2$. The results for each test are gathered in Table 7.

TABLE 7: Confining and shear stress values determined for each test.

Test	Confining stress σ (MPa)	Shear stress τ_{peak} (MPa)	Shear stress τ_{res} (MPa)
TRIPLET_1	0.21	/	/
TRIPLET_2	0.07	0.69	0.4
TRIPLET_3	0.07	0.72	0.4
TRIPLET_4	0.04	0.48	0.26
TRIPLET_5	0.04	0.70	/
TRIPLET_6	0.093	1.09	0.54
TRIPLET_7	0.093	0.88	0.31
TRIPLET_8	0.093	1.22	0.57

This calculation is also repeated for the residual regime, where $F_{i,peak}$ is replaced by $F_{i,res}$, the residual force at the end of the test. In Figure 21, the τ values on the Mohr-Coulomb plane are reported along with a first-order linear approximation of the form $\tau = c + \sigma \tan(\Phi)$, where c is the cohesion and Φ is the friction angle, which are the quantities one aims to determine.

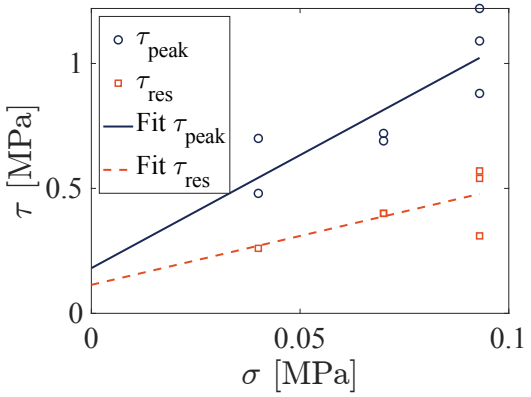

FIGURE 21: Shear stress vs. confining stress loci for all tests at rupture (blue) and in the residual regime (orange).

Ultimately, a cohesion value of $c = 0.18\,\text{MPa}$ is obtained for τ_{peak}, which is relatively low compared to values reported in the literature. In contrast,

the friction angle is estimated at $84°$, which is higher than typical results. For these parameters, and with a confining force similar to that applied in the TRIPLET_1 test, the estimated maximum force is $105\,$kN, consistent with the elastic behavior observed in the initial test. For the residual regime, a cohesion $c = 0.11\,$MPa is obtained for τ_{res}, and the friction angle is estimated at $76°$. It is worth noting that the normative method is highly dependent on the estimation of the shear surface A_i, which evolved over time with the cracking pattern (Figure 11). Additionally, identifying the parameters of the Mohr-Coulomb criterion is challenging, with only a single point per test. Therefore, the approach is to couple force measurements with the evaluation of the shear surface via DIC, enabling for a much larger number of measurement points.

3.2. DIC-based approach

To determine the shear area over time, two cameras are used to measure, at each time step, the uncracked height $h_{\text{uncracked}}$ in both joints of the specimen. For each joint, a band of elements is defined from the mesh. If any of these elements is labelled as damaged at time t, the height of the corresponding band of elements is subtracted from the specimen's total height. The criterion used to determine $h_{\text{uncracked}}$ is the same as the one introduced earlier to assess whether an element was damaged or not. Using this approach, the cracked height in each of the two joints is obtained at time t from both front and rear cameras. The shear area $A_i(t)$ is then defined, per joint, as the average cracked height determined from the two cameras,

multiplied by the thickness e of the specimen:

$$A_i(t) = \frac{h^j_{\text{front,uncracked}}(t) + h^j_{\text{rear,uncracked}}(t)}{2} \cdot e \tag{7}$$

For each test, the shear area $A_i(t)$ is plotted as a function of the image number, allowing the Mohr-Coulomb criterion to be deduced from Equation (6) for a given configuration (Figure 22). Once the sum of the area $A_i(t)$ for both joints becomes smaller than a threshold value, here 0.015 m^2, the residual regime is assumed to be reached. This value was chosen to correspond to 80% of the cracked area. Experimentally, it is observed that beyond this threshold, the central block slides along the two other blocks, making the behavior primarily governed by friction. In this regime, the same equations are applied, replacing the shear area with $A_{\text{res}}(t) = A_i(0) - A_i(t)$. By repeating this procedure for all the tests conducted during the experimental campaign, it becomes possible to plot, in the Mohr plane, all the measurement points obtained through the coupling of DIC and force measurements both prior to complete failure and in the residual regime (Figure 23).

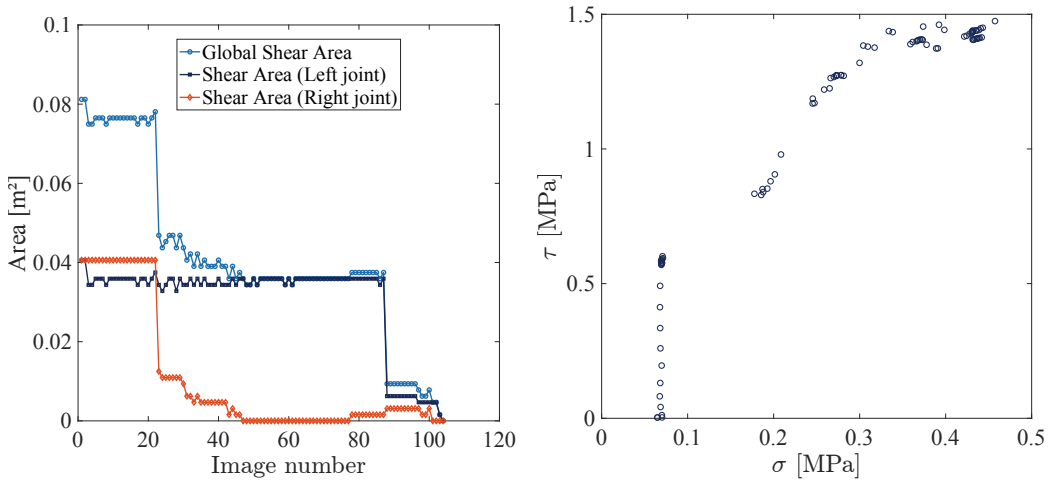

FIGURE 22: Evolution of the shear area as a function of the image number (a) and Mohr-Coulomb criterion derived from Test 2 data (b).

Regarding the data prior to complete failure, it is interesting to note the clear emergence of the Mohr-Coulomb criterion, which is globally validated for all tests (Figure 23). Only the TRIPLET_2, TRIPLET_6, TRIPLET_7, and TRIPLET_8 tests reached the residual regime. This behavior is consistent with previous observations, as the other tests showed no failure in either joint. An exception is observed in the TRIPLET_4 test, where both joints exhibit cracking. However, the damage criterion indicates that certain areas in the left joint are not completely damaged, preventing A_i from falling below the threshold value.

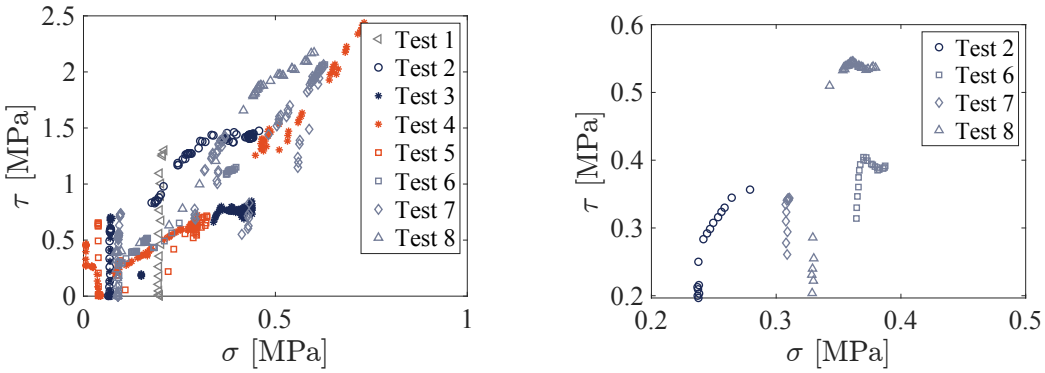

FIGURE 23: Evolution of shear stress as a function of confining stress prior to complete failure (a) and in the residual regime (b).

The objective is now to determine the Mohr-Coulomb line while excluding outliers. The upper quantiles (95th percentile) of τ are calculated within each bin of σ. A Mohr-Coulomb envelope is then fitted by adjusting a linear equation of the form $\tau = c + \sigma \cdot \tan(\phi)$ to these quantile points, providing a representative criterion. The envelope is computed and superimposed on the overall scatter plot of data points (Figure 24). One finally finds a cohesion of 0.45 MPa and a friction angle of 70°.

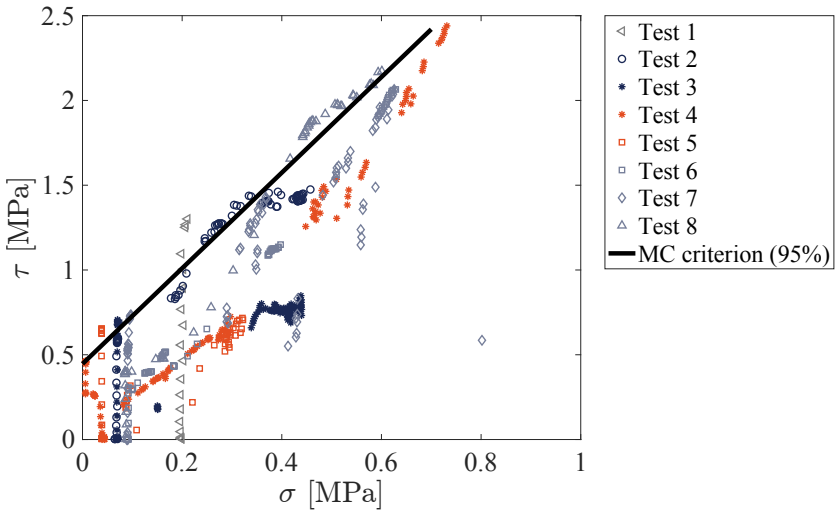

FIGURE 24: Mohr-Coulomb criterion derived from DIC and force measurements.

The Mohr-Coulomb parameters identified using DIC are consistent with those traditionally reported in the literature. Compared to the normative approach, the number of evaluation points is increased by a factor of 100, allowing for greater confidence in the obtained results. The results in Figure 24 include the experimental observations. It is worth noting that at least six different tests contribute to defining the envelope, highlighting the robustness of the criterion.

For the TRIPLET_1 test, the final values exceed a bit the failure criterion, which coincides with the first discontinuities appearing in the displacement field (Figure 7a). For the TRIPLET_2 and TRIPLET_8 tests, the first joint fractures after reaching the failure criterion, and the shear stress increases with the applied normal force, following the Mohr-Coulomb line until cracking occurs in the second joint.

For the TRIPLET_3, TRIPLET_5, and TRIPLET_7 tests, cracking in the first joint occurred at values slightly above the criterion, after which the

values remained below the criterion, explaining why cracking did not initiate in the second joint. In the TRIPLET_4 test, after the first cracking event, the values increase and approach the maximum level of the criterion without reaching it, which explains why the residual regime was not achieved. Last, for the TRIPLET_6 test, the values after the first cracking event remained below the criterion. However, cracking occurred in concrete, which was not expected according to the defined criterion.

To discuss studies highlighting the complexities of analyzing triplet tests, particularly after peak displacements, due to the simultaneous testing of two joints [36, 22], DIC offers the opportunity to understand post-peak failure better and provides more consistent results.

Determining a friction model for the entire surface in the residual regime is more challenging due to limited data and the scarcity of tests that reach this regime. The residual friction angle is found to be 60°, which is consistent since the static friction angle is lower than the dynamic friction angle determined by the Mohr-Coulomb criterion.

4. Conclusion

This paper explored the possibilities offered by DIC for investigating the shear behavior of masonry triplets. Using monoview DIC with two cameras positioned on either side, coupled with precise force and confining stress measurements, allows for a better characterization of the phenomena occurring during shear triplet tests. The main advantage is the ability to compare the evolution of the force-displacement curve with the displacement field measurements, particularly to identify local phenomena that may not

have been detected otherwise. The measurement of the expansion of the joints is now performed globally, enabling for the evaluation of the MCOD for each joint. This approach allows for the characterization of the cohesive and adhesive behavior, along with a mesoscopic quantification of damage.

The previous data were used to more accurately identify the parameters of the Mohr-Coulomb failure criterion by compiling data from all the reported tests. The proposed approach involved determining the cracked height at each image based on a damage criterion, allowing for a precise determination of the shear area and, consequently, the evaluation at each time step of a point in the Mohr-Coulomb plane. This method differs from normative approaches that typically use only a few points per test.

The obtained results confirm the robustness of the method applied to the eight shear tests performed for various confinement stresses. Future work will focus on comparing this rich experimental data set with the numerical modeling of these tests, particularly with the possibility of accounting for the boundary conditions actually prescribed during the model updating phase.

Regarding the DIC calculation, a choice was made not to split the nodes at the interface between the mortar and the concrete, even though it would improve the DIC displacement field by avoiding gradients at the interface. This decision was made because the long-term goal is to perform model updating with finite element models that do not account for this jump at the interface. Yet, it is possible to refine the analyses even more from a pure measurement viewpoint.

Acknowledgments

The ERMES Department of EDF R&D and the École Normale Supérieure Paris Saclay (ENS Paris Saclay) are kindly thanked for financial supports. The research reported in this paper has been supported in part by the SEISM Paris Saclay Research Institute. Special thanks are extended to the experimental team, including Xavier Pinelli, Olivier Rateau, and Laëticia Szturycz, for their invaluable assistance in implementing the experimental setup.

Appendix A. DIC Global formulation

The displacement field $\mathbf{u}(\mathbf{x})$ is determined via non-linear least squares minimization of the global gray level residual

$$C_1 = \int_R [f(\mathbf{x}) - g(\mathbf{x} + \mathbf{u}(\mathbf{x}))]^2 \mathbf{dx} \tag{A.1}$$

The DIC cost function, Φ^2_{DIC}, can be defined with σ as the standard deviation of acquisition noise, which is assumed to be white and Gaussian

$$\Phi^2_{DIC} = \frac{1}{2\sigma^2} C_1 \tag{A.2}$$

The global approach enables for the use of a continuous transformation basis, such as the Finite Element (FE) formulation [17]. In this context, the displacement field $\mathbf{u}(\mathbf{x})$ is expressed as a linear combination of spatial shape

functions $\mathbf{\Phi}_i$

$$\mathbf{u}(\mathbf{x}, \mathbf{t}) = \sum_{i}^{N_n} v_i(t)\mathbf{\Phi}_i(\mathbf{x}) \tag{A.3}$$

where $v_i(t)$ represents the nodal displacement to be determined at each time step t for the i-th nodes.

Appendix A.1. Brightness and Contrast Corrections (BCCs)

The tests on the triplets lasted an average of two hours. Despite isolating the test environment with black sheets and controlling the lighting with several spotlights, it was still necessary to account for potential variations in brightness and contrast that could influence the measurements. BCCs relax the brightness conservation equation (1), allowing for smooth changes in brightness and contrast fields. It is carried out by finding the best match between the gray levels of the two registered images [17]. The new global gray level residuals become

$$C_2 = \int_R [(1 + c(\mathbf{x}))\, f(\mathbf{x}) + b(\mathbf{x}) - g(\mathbf{x} + \mathbf{u}(\mathbf{x}))]^2 \mathbf{dx} \tag{A.4}$$

$$\Phi^2_{DIC,BCC} = \frac{1}{2\sigma^2} C_2 \tag{A.5}$$

Minimizing this quantity results in the updating of the correction fields $b(\mathbf{x})$ and $c(\mathbf{x})$, which are interpreted as changes in brightness and contrast, respectively, of the image between the two configurations. These fields are expressed as a linear combination of spatial shape function Φ_i.

The global minimization of the cost function (Equation A.5) is conducted through an iterative two-step process that alternates updating of displacements and BC fields.

Appendix A.2. Mechanical regularization

DIC is considered an ill-posed problem in the sense defined by Hadamard. This observation means that the finite element discretization cannot be made arbitrarily fine, as doing so would significantly increase the measurement uncertainties [19]. To tackle this challenge, mechanical regularization is introduced [27, 35], effectively filtering out displacement fluctuations that are not mechanically admissible. A penalty term is incorporated into the DIC cost function based on the equilibrium gap [10]

$$\Phi_m^2 = \{\mathbf{v}\}^T[\mathbf{K}]^T[\mathbf{K}]\{\mathbf{v}\} \tag{A.6}$$

where $[\mathbf{K}]$ is the stiffness matrix. This penalization is applied to inner nodes and force-free boundaries. For Dirichlet boundary nodes, another regularization is necessary, where a penalization of short wavelength traction fluctuations is performed

$$\Phi_b^2 = \{\mathbf{v}\}^T[\mathbf{K}]^T[\mathbf{L}][\mathbf{K}]\{\mathbf{v}\} \tag{A.7}$$

where $[\mathbf{L}]$ is the Laplace-Beltrami operator [23]. The total cost function Φ_t^2 is introduced when the correlation residuals $\Phi_{DIC,BCC}^2$, equilibrium gap Φ_m^2,

and boundary fluctuations Φ_b^2 are minimized simultaneously

$$\{\mathbf{v}\}_{reg} = \arg\min\left(\Phi_{DIC,BCC}^2 + w_m\Phi_m^2 + w_b\Phi_b^2\right) \tag{A.8}$$

where w_m and w_b are the corresponding weights, which are proportional to regularization lengths ℓ_m and ℓ_b raised to the power 4 [27].

References

[1] AFNOR, 2012. Essais pour béton durci - partie 6 : détermination de la résistance en traction par fendage d'éprouvettes .

[2] AFNOR, 2014. Essai pour béton durci - partie 13 : détermination du module sécant d'élasticité en compression .

[3] AFNOR, 2019. Essais pour béton durci - partie 3 : résistance à la compression des éprouvettes .

[4] Andreotti, G., Graziotti, F., Magenes, G., 2018. Detailed micro-modelling of the direct shear tests of brick masonry specimens: The role of dilatancy. Engineering Structures 168, 929–949. URL: https://www.sciencedirect.com/science/article/pii/S0141029617322150, doi:https://doi.org/10.1016/j.engstruct.2018.05.019.

[5] Barattucci, S., Sarhosis, V., Bruno, A.W., D'Altri, A.M., de Miranda, S., Castellazzi, G., 2020. An experimental and numerical study on masonry triplets subjected to monotonic and cyclic shear loadings. Construction and Building Materials

254, 119313. URL: https://www.sciencedirect.com/science/article/pii/S0950061820313180, doi:https://doi.org/10.1016/j.conbuildmat.2020.119313.

[6] Belliazzi, S., Fabbrocino, F., Lignola, G.P., Prota, A., 2024. Advantages of using dic for capturing mechanical shear sliding behaviour of the frcm strengthened masonry. Structures 68, 107056. URL: https://www.sciencedirect.com/science/article/pii/S2352012424012086, doi:https://doi.org/10.1016/j.istruc.2024.107056.

[7] Bompa, D., Elghazouli, A., 2020. Experimental and numerical assessment of the shear behaviour of lime mortar clay brick masonry triplets. Construction and Building Materials 262, 120571. URL: https://www.sciencedirect.com/science/article/pii/S0950061820325769, doi:https://doi.org/10.1016/j.conbuildmat.2020.120571.

[8] Calderón, S., Sandoval, C., Araya-Letelier, G., Aguilar, V., 2023. A detailed experimental mechanical characterization of multi-perforated clay brick masonry. Journal of Building Engineering 63, 105505. URL: https://www.sciencedirect.com/science/article/pii/S235271022201511X, doi:https://doi.org/10.1016/j.jobe.2022.105505.

[9] Chang, X., Le Gourriérec, C., Hild, F., Roux, S., 2024. Brightness and contrast corrections for stereocorrelation: Global and instantaneous

formulation with spatial regularization. Mechanical Systems and Signal Processing 208, 111057. URL: https://www.sciencedirect.com/science/article/pii/S0888327023009652, doi:https://doi.org/10.1016/j.ymssp.2023.111057.

[10] Claire, D., Hild, F., Roux, S., . A finite element formulation to identify damage fields: the equilibrium gap method. International Journal for Numerical Methods in Engineering 61, 189–208. URL: https://onlinelibrary.wiley.com/doi/abs/10.1002/nme.1057, doi:https://doi.org/10.1002/nme.1057.

[11] Collin, L., Gatuingt, F., Giry, C., Hervé-Secourgeon, G., 2024. Establishing a test-calculation dialogue for shear tests on masonry triplets. Academic Journal of Civil Engineering 42, 426–436. URL: https://journal.augc.asso.fr/index.php/ajce/article/view/4745, doi:10.26168/ajce.42.1.38.

[12] Collin, L., Gatuingt, F., Giry, C., Hild, F., 2025. Virtual Design of Masonry Triplet Shear Tests using Digital Image Correlation. Materials and structures 58, 203. URL: https://hal.science/hal-05118956, doi:10.1617/s11527-025-02707-9.

[13] Dais, D., İhsan Engin Bal, Smyrou, E., Sarhosis, V., 2021. Automatic crack classification and segmentation on masonry surfaces using convolutional neural networks and transfer learning. Automation in Construction 125, 103606. URL: https://www.sciencedirect.com/science/article/pii/S0926580521000571, doi:https://doi.org/10.1016/j.autcon.2021.103606.

[14] Dhanasekar, M., Page, A., Kleeman, P., 1985. The failure of brick masonry under biaxial stresses. Proceedings of the Institution of Civil Engineers 79, 295–313. URL: https://doi.org/10.1680/iicep.1985.992, doi:10.1680/iicep.1985.992.

[15] Dhir, P.K., Tubaldi, E., Orfeo, A., Ahmadi, H., 2022. Cyclic shear behaviour of masonry triplets with rubber joints. Construction and Building Materials 351, 128356. URL: https://www.sciencedirect.com/science/article/pii/S0950061822020165, doi:https://doi.org/10.1016/j.conbuildmat.2022.128356.

[16] Ghorbani, R., Matta, F., Sutton, M.A., 2015. Full-field deformation measurement and crack mapping on confined masonry walls using digital image correlation. Experimental Mechanics 55, 227–243. doi:https://doi.org/10.1007/s11340-014-9906-y.

[17] Grédiac, M., Hild, F., 2012. Full-field measurements and identification in solid mechanics. John Wiley & Sons. URL: https://onlinelibrary.wiley.com/doi/abs/10.1002/9781118578469.fmatter, doi:https://doi.org/10.1002/9781118578469.fmatter.

[18] Guerrero, N., Martinez, M., Picón, R., Marante, M.E., Hild, F., Roux, S., Flórez-López, J., 2014. Experimental analysis of masonry infilled frames using digital image correlation. Materials and structures 47, 873–884. doi:https://doi.org/10.1617/s11527-013-0099-0.

[19] Hild, F., Roux, S., 2012. Comparison of local and global approaches

to digital image correlation. Experimental mechanics 52, 1503–1519. doi:https://doi.org/10.1007/s11340-012-9603-7.

[20] Horn, B.K., Schunck, B.G., 1981. Determining optical flow. Artificial Intelligence 17, 185–203. URL: https://www.sciencedirect.com/science/article/pii/0004370281900242, doi:https://doi.org/10.1016/0004-3702(81)90024-2.

[21] Leclerc, H., Neggers, J., Mathieu, F., Hild, F., Roux, S., 2015. Correli 3.0. Iddn. fr 1.

[22] Lourenço, P., Barros, J., Oliveira, J., 2004. Shear testing of stack bonded masonry. Construction and Building Materials 18, 125–132. URL: https://www.sciencedirect.com/science/article/pii/S0950061803000722, doi:https://doi.org/10.1016/j.conbuildmat.2003.08.018.

[23] Mendoza, A., Schneider, J., Parra, E., Roux, S., 2019. The correlation framework: Bridging the gap between modeling and analysis for 3d woven composites. Composite Structures 229, 111468. URL: https://www.sciencedirect.com/science/article/pii/S0263822318346221, doi:https://doi.org/10.1016/j.compstruct.2019.111468.

[24] Petry, S., Beyer, K., 2014. Cyclic test data of six unreinforced masonry walls with different boundary conditions. Earthquake Spectra 31, 2459–2484. doi:10.1193/101513EQS269.

[25] Raffard, D., Ienny, P., Henry, J., 2001. Displacement and strain fields at a stone/mortar interface by digital image processing. Journal of Testing and Evaluation 29, 115–122. doi:10.1520/JTE12237J.

[26] Riddington, J.R., Jukes, P., 1994. A comparison between panel, joint and code shear strength, in: 10th Int. Brick Block Mason. Conf., Masonry Council of Canada, pp. 1481–1490.

[27] Réthoré, J., Roux, S., and, F.H., 2009. An extended and integrated digital image correlation technique applied to the analysis of fractured samples. European Journal of Computational Mechanics 18, 285–306. URL: https://doi.org/10.3166/ejcm.18.285-306, doi:10.3166/ejcm.18.285-306.

[28] Sciuti, V., Hild, F., Pandolfelli, V., Santos, T., Smaniotto, B., Canto, R., 2021. Digital image correlation applied to in situ evaluation of surface cracks upon curing of mgo-containing refractory castables. Journal of the European Ceramic Society 41, 1003–1014. URL: https://www.sciencedirect.com/science/article/pii/S0955221920303460, doi:https://doi.org/10.1016/j.jeurceramsoc.2020.04.055.

[29] Sciuti, V.F., Vargas, R., Guerrero, N., Marante, M.E., Hild, F., 2025. Digital image correlation analyses of masonry infilled frame: Uncertainty-based mesh refinement and damage quantification. Mathematics and Mechanics of Solids 30, 93–115. URL: https://doi.org/10.1177/10812865231174840, doi:10.1177/10812865231174840.

[30] Segura, J., Bernat, E., Mendizábal Dinucci, V., Pelà, L., Roca, P., Gil, L., 2021. Experimental comparison of two testing setups for characterizing the shear mechanical properties of masonry. Journal of Building Engineering 44, 103277. doi:10.1016/j.jobe.2021.103277.

[31] Shih, M.H., Tung, S.H., Kuo, J.C., Sung, W.P., 2006. The application of a digital image correlation method for crack observation. doi:10.4203/ccp.83.86.

[32] for Standardization, E.C., 1999. En 1015-11, methods of test for mortar for masonry. determination of flexural and compressive strength of hardened mortar. Brussels, Belgium .

[33] for Standardization, E.C., 2002. En 1052-3: 2002; methods of test for masonry—part 3: Determination of initial shear strength. Brussels, Belgium .

[34] Thamboo, J.A., Dhanasekar, M., Yan, C., 2013. Flexural and shear bond characteristics of thin layer polymer cement mortared concrete masonry. Construction and Building Materials 46, 104–113. URL: https://www.sciencedirect.com/science/article/pii/S0950061813003073, doi:https://doi.org/10.1016/j.conbuildmat.2013.04.002.

[35] Tomicevic, Z., Hild, F., Roux, S., 2013. Mechanics-aided digital image correlation. The Journal of Strain Analysis for Engineering Design 48, 330–343. doi:10.1177/0309324713482457.

[36] Vasconcelos, G., Lourenço, P.B., Oliveira, D.V., 2008. Experimental shear behavior of stone masonry joints, in: Structural Analysis of Historic Construction, Taylor and Francis. pp. 771–779.